Research Article | Vol. 9, No. 9 | 1 Sep 2018 | BIOMEDICAL OPTICS EXPRESS 4372
Biomedical Optics EXPRESS

# Clinical prototype of pigment and flow imaging optical coherence tomography for posterior eye investigation

**Shuichi Makita,[1*] Toshihiro Mino,[2] Tastuo Yamaguchi,[2] Mashiro Miura,[3] Shinnosuke Azuma,[1] and Yoshiaki Yasuno[1]**

[1] *Computational Optics Group, University of Tsukuba, 1-1-1 Tennodai, Tsukuba, Ibaraki 305-8573, Japan*
[2] *Topcon Corporation, 75-1 Hasunumacho, Itabashi, Tokyo 174-8580, Japan*
[3] *Department of Ophthalmology, Tokyo Medical University Ibaraki Medical Center, 3-20-1 Chuo, Ami, Ibaraki 300-0395, Japan*
[*] *makita@optlab2.bk.tsukuba.ac.jp*
*http://optics.bk.tsukuba.ac.jp*

**Abstract:** Measurements of the randomness of polarization (RP) obtained using polarization-sensitive optical coherence tomography (PS-OCT) are applied in several applications, and RP is attractive for posterior eye imaging. The addition of RP without retardation requires a minimal extension to standard OCT; therefore, we developed a prototype OCT system with a simplified scheme for RP measurement. A compact polarization-diversity receiver module is the only required hardware extension to a standard OCT system. All components were packed into the retinal scanning head. The degree-of-polarization uniformity and complex-decorrelation based OCT angiography were calculated using noise-corrected algorithms that accounted for the depth-dependent noise power. The structure, melanin, and blood flow distribution imaging of *in vivo* human eyes were demonstrated. Pathological eye imaging shows potential applications for combinations of these contrasts.



**OCIS codes:** (170.4500) Optical coherence tomography; (170.4470) Ophthalmology; (120.3890) Medical optics instrumentation.

## References and links

1. E. Götzinger, M. Pircher, W. Geitzenauer, C. Ahlers, B. Baumann, S. Michels, U. Schmidt-Erfurth, and C. K. Hitzenberger, "Retinal pigment epithelium segmentation by polarization sensitive optical coherence tomography," Opt. Express **16**, 16410–16422 (2008).
2. B. Baumann, S. O. Baumann, T. Konegger, M. Pircher, E. Götzinger, F. Schlanitz, C. Schütze, H. Sattmann, M. Litschauer, U. Schmidt-Erfurth, and C. K. Hitzenberger, "Polarization sensitive optical coherence tomography of melanin provides intrinsic contrast based on depolarization," Biomed. Opt. Express **3**, 1670–1683 (2012).
3. S. Makita, Y.-J. Hong, M. Miura, and Y. Yasuno, "Degree of polarization uniformity with high noise immunity using polarization-sensitive optical coherence tomography," Opt. Lett. **39**, 6783–6786 (2014).
4. M. Yamanari, S. Tsuda, T. Kokubun, Y. Shiga, K. Omodaka, N. Aizawa, Y. Yokoyama, N. Himori, S. Kunimatsu-Sanuki, K. Maruyama, H. Kunikata, and T. Nakazawa, "Estimation of Jones matrix, birefringence and entropy using Cloude-Pottier decomposition in polarization-sensitive optical coherence tomography," Biomed. Opt. Express **7**, 3551–3573 (2016).
5. W. C. Y. Lo, M. Villiger, A. Golberg, G. F. Broelsch, S. Khan, C. G. Lian, W. G. Austen Jr., M. Yarmush, and B. E. Bouma, "Longitudinal, 3D imaging of collagen remodeling in murine hypertrophic scars *in vivo* using polarization-sensitive optical frequency domain imaging," J. Invest. Dermatol. **136**, 84–92 (2016).
6. M. Yamanari, K. Ishii, S. Fukuda, Y. Lim, L. Duan, S. Makita, M. Miura, T. Oshika, and Y. Yasuno, "Optical rheology of porcine sclera by birefringence imaging," PLoS ONE **7**, e44026 (2012).
7. J. Golde, F. Tetschke, J. Walther, T. Rosenauer, F. Hempel, and C. Hannig, "Detection of carious lesions utilizing depolarization imaging by polarization sensitive optical coherence tomography," J. Biomed. Opt. **23**, 041203 (2018).
8. J. Lammer, M. Bolz, B. Baumann, M. Pircher, B. Gerendas, F. Schlanitz, C. K. Hitzenberger, and U. Schmidt-Erfurth, "Detection and analysis of hard exudates by polarization-sensitive optical coherence tomography in patients with diabetic maculopathy," Invest. Ophthalmol. Vis. Sci. **55**, 1564–1571 (2014).
9. R. G. Sayegh, S. Zotter, P. K. Roberts, M. M. Kandula, S. Sacu, D. P. Kreil, B. Baumann, M. Pircher, C. K. Hitzenberger, and U. Schmidt-Erfurth, "Polarization-sensitive optical coherence tomography and conventional retinal

#331931 https://doi.org/10.1364/BOE.9.004372
Journal © 2018 Received 14 Jun 2018; revised 10 Aug 2018; accepted 10 Aug 2018; published 20 Aug 2018

Biomedical Optics EXPRESS

imaging strategies in assessing foveal integrity in geographic atrophy," Invest. Ophthalmol. Vis. Sci. **56**, 5246–5255 (2015).
10. P. Roberts, B. Baumann, J. Lammer, B. Gerendas, J. Kroisamer, W. Bühl, M. Pircher, C. K. Hitzenberger, U. Schmidt-Erfurth, and S. Sacu, "Retinal pigment epithelial features in central serous chorioretinopathy identified by polarization-sensitive optical coherence tomography," Invest. Ophthalmol. Vis. Sci. **57**, 1595–1603 (2016).
11. P. K. Roberts, B. Baumann, F. G. Schlanitz, S. Sacu, M. Bolz, M. Pircher, M. Hagmann, C. K. Hitzenberger, and U. Schmidt-Erfurth, "Retinal pigment epithelial features indicative of neovascular progression in age-related macular degeneration," Br. J. Ophthalmol. **101**, 1361–1366 (2017).
12. M. Miura, S. Makita, Y. Yasuno, R. Tsukahara, Y. Usui, N. A. Rao, Y. Ikuno, S. Uematsu, T. Agawa, T. Iwasaki, and H. Goto, "Polarization-sensitive optical coherence tomographic documentation of choroidal melanin loss in chronic Vogt–Koyanagi–Harada disease," Invest. Ophthalmol. Vis. Sci. **58**, 4467–4476 (2017).
13. M. Miura, S. Makita, S. Sugiyama, Y.-J. Hong, Y. Yasuno, A. E. Elsner, S. Tamiya, R. Tsukahara, T. Iwasaki, and H. Goto, "Evaluation of intraretinal migration of retinal pigment epithelial cells in age-related macular degeneration using polarimetric imaging," Sci. Rep. **7**, 3150 (2017).
14. M. R. Hee, D. Huang, E. A. Swanson, and J. G. Fujimoto, "Polarization-sensitive low-coherence reflectometer for birefringence characterization and ranging," J. Opt. Soc. Am. B **9**, 903–908 (1992).
15. C. Hitzenberger, E. Götzinger, M. Sticker, M. Pircher, and A. Fercher, "Measurement and imaging of birefringence and optic axis orientation by phase resolved polarization sensitive optical coherence tomography," Opt. Express **9**, 780–790 (2001).
16. E. Götzinger, B. Baumann, M. Pircher, and C. K. Hitzenberger, "Polarization maintaining fiber based ultra-high resolution spectral domain polarization sensitive optical coherence tomography," Opt. Express **17**, 22704–22717 (2009).
17. W. Trasischker, S. Zotter, T. Torzicky, B. Baumann, R. Haindl, M. Pircher, and C. K. Hitzenberger, "Single input state polarization sensitive swept source optical coherence tomography based on an all single mode fiber interferometer," Biomed. Opt. Express **5**, 2798–2809 (2014).
18. N. Lippok, M. Villiger, C. Jun, and B. E. Bouma, "Single input state, single-mode fiber-based polarization-sensitive optical frequency domain imaging by eigenpolarization referencing," Opt. Lett. **40**, 2025–2028 (2015).
19. S. Makita, M. Yamanari, and Y. Yasuno, "Generalized Jones matrix optical coherence tomography: Performance and local birefringence imaging," Opt. Express **18**, 854–876 (2010).
20. J. F. de Boer and T. E. Milner, "Review of polarization sensitive optical coherence tomography and Stokes vector determination," J. Biomed. Opt. **7**, 359–371 (2002).
21. M. Yamanari, S. Makita, and Y. Yasuno, "Polarization-sensitive swept-source optical coherence tomography with continuous source polarization modulation," Opt. Express **16**, 5892–5906 (2008).
22. Y. Lim, Y.-J. Hong, L. Duan, M. Yamanari, and Y. Yasuno, "Passive component based multifunctional Jones matrix swept source optical coherence tomography for Doppler and polarization imaging," Opt. Lett. **37**, 1958–1960 (2012).
23. B. Baumann, W. Choi, B. Potsaid, D. Huang, J. S. Duker, and J. G. Fujimoto, "Swept source / Fourier domain polarization sensitive optical coherence tomography with a passive polarization delay unit," Opt. Express **20**, 10229–10241 (2012).
24. W. Oh, S. Yun, B. Vakoc, M. Shishkov, A. Desjardins, B. Park, J. de Boer, G. Tearney, and B. Bouma, "High-speed polarization sensitive optical frequency domain imaging with frequency multiplexing," Opt. Express **16**, 1096–1103 (2008).
25. S. Guo, J. Zhang, L. Wang, J. S. Nelson, and Z. Chen, "Depth-resolved birefringence and differential optical axis orientation measurements with fiber-based polarization-sensitive optical coherence tomography," Opt. Lett. **29**, 2025–2027 (2004).
26. M. Todorović, S. Jiao, L. V. Wang, and G. Stoica, "Determination of local polarization properties of biological samples in the presence of diattenuation by use of Mueller optical coherence tomography," Opt. Lett. **29**, 2402–2404 (2004).
27. C. Fan and G. Yao, "Mapping local retardance in birefringent samples using polarization sensitive optical coherence tomography," Opt. Lett. **37**, 1415–1417 (2012).
28. E. Li, S. Makita, Y.-J. Hong, D. Kasaragod, and Y. Yasuno, "Three-dimensional multi-contrast imaging of in vivo human skin by Jones matrix optical coherence tomography," Biomed. Opt. Express **8**, 1290–1305 (2017).
29. S. Moon, S.-W. Lee, and Z. Chen, "Reference spectrum extraction and fixed-pattern noise removal in optical coherence tomography," Opt. Express **18**, 24395–24404 (2010).
30. S. Makita, K. Kurokawa, Y.-J. Hong, M. Miura, and Y. Yasuno, "Noise-immune complex correlation for optical coherence angiography based on standard and Jones matrix optical coherence tomography," Biomed. Opt. Express **7**, 1525–1548 (2016).
31. M. Villiger, D. Lorenser, R. A. McLaughlin, B. C. Quirk, R. W. Kirk, B. E. Bouma, and D. D. Sampson, "Deep tissue volume imaging of birefringence through fibre-optic needle probes for the delineation of breast tumour," Sci. Rep. **6**, 28771 (2016).
32. S. Dithmar and F. G. Holz, *Fluorescence Angiography in Ophthalmology* (Springer, 2008).
33. P. Thévenaz and M. Unser, "User-friendly semiautomated assembly of accurate image mosaics in microscopy," Microsc. Res. Tech. **70**, 135–146 (2007).
34. J. Schindelin, I. Arganda-Carreras, E. Frise, V. Kaynig, M. Longair, T. Pietzsch, S. Preibisch, C. Rueden, S. Saalfeld,

Biomedical Optics EXPRESS

B. Schmid, J.-Y. Tinevez, D. J. White, V. Hartenstein, K. Eliceiri, P. Tomancak, and A. Cardona, "Fiji: An open-source platform for biological-image analysis," Nat. Methods **9**, 676–682 (2012).
35. S. Azuma, S. Makita, A. Miyazawa, Y. Ikuno, M. Miura, and Y. Yasuno, "Pixel-wise segmentation of severely pathologic retinal pigment epithelium and choroidal stroma using multi-contrast Jones matrix optical coherence tomography," Biomed. Opt. Express **9**, 2955–2973 (2018).
36. M. J. Ju, Y.-J. Hong, S. Makita, Y. Lim, K. Kurokawa, L. Duan, M. Miura, S. Tang, and Y. Yasuno, "Advanced multi-contrast Jones matrix optical coherence tomography for Doppler and polarization sensitive imaging," Opt. Express **21**, 19412–19436 (2013).
37. N. Lippok, M. Villiger, and B. E. Bouma, "Degree of polarization (uniformity) and depolarization index: Unambiguous depolarization contrast for optical coherence tomography," Opt. Lett. **40**, 3954–3957 (2015).
38. N. Lippok, M. Villiger, A. Albanese, E. F. J. Meijer, K. Chung, T. P. Padera, S. N. Bhatia, and B. E. Bouma, "Depolarization signatures map gold nanorods within biological tissue," Nat. Photonics **11**, 583–588 (2017).
39. R. W. Knighton and X.-R. Huang, "Linear birefringence of the central human cornea," Invest. Ophthalmol. Vis. Sci. **43**, 82–86 (2002).
40. R. W. Knighton, X.-R. Huang, and L. A. Cavuoto, "Corneal birefringence mapped by scanning laser polarimetry," Opt. Express **16**, 13738–13751 (2008).
41. H. B. klein Brink and G. J. van Blokland, "Birefringence of the human foveal area assessed in vivo with Mueller-matrix ellipsometry," J. Opt. Soc. Am. A **5**, 49–57 (1988).
42. A. E. Elsner, A. Weber, M. C. Cheney, and D. A. VanNasdale, "Spatial distribution of macular birefringence associated with the Henle fibers," Vis. Res. **48**, 2578–2585 (2008).
43. B. Cense, Q. Wang, S. Lee, L. Zhao, A. E. Elsner, C. K. Hitzenberger, and D. T. Miller, "Henle fiber layer phase retardation measured with polarization-sensitive optical coherence tomography," Biomed. Opt. Express **4**, 2296–2306 (2013).
44. T. Fabritius, S. Makita, M. Miura, R. Myllylä, and Y. Yasuno, "Automated segmentation of the macula by optical coherence tomography," Opt. Express **17**, 15659–15669 (2009).
45. Y. Chen, Y.-J. Hong, S. Makita, and Y. Yasuno, "Eye-motion-corrected optical coherence tomography angiography using Lissajous scanning," Biomed. Opt. Express **9**, 1111–1129 (2018).

## 1. Introduction

The additional contrast available with optical coherence tomography (OCT) allows extended applications, for example, OCT angiography (OCT-A), which enables the development of microvasculature imaging applications. Recently, various metrics of the randomness of polarization (RP) have been demonstrated in several fields. The degree of polarization uniformity (DOPU) [1–3] and polarization entropy [4] allow the visualization of the distribution of melanin. DOPU [5] and the degree of axis orientation uniformity [6] are used to contrast the randomness of collagen orientation in tissues, for example, skin and sclera of the eye. DOPU is also used to contrast carious lesions [7]. In ophthalmology, DOPU is widely studied for the retinal pigment epithelium (RPE) imaging of both healthy and pathological eyes [8–13]. RP is one of the contrasts obtained in polarization-sensitive OCT (PS-OCT). Historically, RP has been considered as a secondary contrast of PS-OCT, whereas phase retardation or birefringence is considered as the primary contrast of interest.

To achieve phase retardation measurement, more elaborate hardware and software are required compared with those for standard OCT. In the case of a circularly polarized input algorithm [14], the polarization state of light should be precisely controlled. Thus, in addition to a polarization-diversity receiver (PDR), a bulk optics [15] or polarization-maintaining fiber-based interferometer [16] is required. Alternatively, in the case of a single-mode (SM) fiber-based system, careful alignment of the fiber polarization property [17, 18] is required. Jones-matrix [19] and Stokes-vector-based algorithms [20] use multiple input polarization states, which avoid the necessity of a circular polarization state for incident light on tissues. However, the use of two input polarization states requires an additional mechanism of polarization multiplexing, such as polarization modulation (electro-optic modulator) [21], path-length multiplexing [22, 23], or frequency multiplexing [24]. In addition to these hardware extensions, complicated algorithms to extract local phase retardation / birefringence [19, 25–27] are required to contrast birefringent tissues.

The measurement of only the RP parameter without phase retardation, particularly using DOPU,

Biomedical Optics EXPRESS

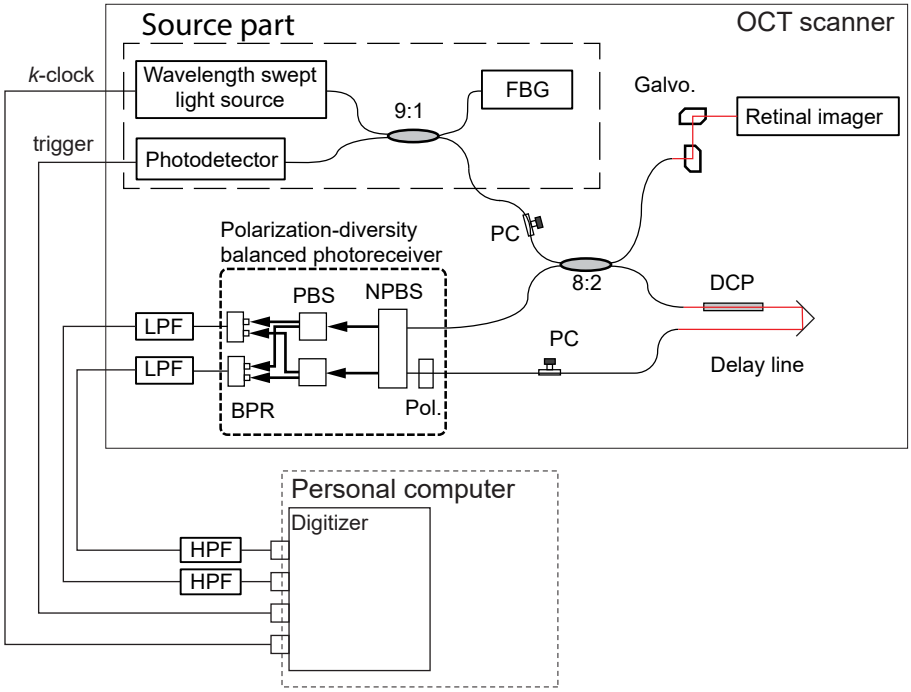


Fig. 1. Schematic diagram of the PAF-OCT system. PC: Polarization controller, FBG: fiber Bragg grating, NPBS: non-polarization beam splitter, PBS: polarization beam splitter, LPF: low-pass filter, HPF: high-pass filter, DCP: dispersion compensation material.

requires a minimal extension to standard OCT. The minimal additional hardware complexity required for only DOPU measurement is introduction of the PDR. Moreover, several studies have focused solely on RP, and report its usefulness in several clinical applications of PS-OCT to the posterior eye [8–13].

Regarding the usefulness of RP and minimal hardware complexity requirement, it would be rational to develop a simple OCT system for posterior eye investigation that could measure DOPU but not phase retardation. In this paper, we demonstrate a clinical prototype of a pigment and flow imaging OCT (PAF-OCT) system. The entire system, except the personal computer, is packed into a standard-sized OCT retinal scanner. Although this OCT cannot measure phase retardation/birefringence, it simultaneously measures DOPU, OCT, and OCT-A, that is, a single scan with this OCT provides information on structural, vascular, and RPE disorders.

The hardware design and computation methods for OCT, OCT-A, and DOPU for this PAF-OCT are described in Sections 2.1 and 2.2. The image formation methods for *en face* pigment and flow visualization are described in Section 3.2. Additionally, the clinical utility of this PAF-OCT system is discussed by presenting the results from some pathological cases.

## 2. Methods

### 2.1. Clinical prototype of PAF-OCT

A schematic diagram of the PAF-OCT system is shown in Fig. 1. A wavelength swept source at a 1-$\mu$m wavelength band with a sweep rate of 100 kHz (Axsun Technologies, MA, USA) is used. Ten percent of the light is split and generates a trigger with a fiber Bragg grating (FBG, 40 % reflectivity at 996 nm wavelength, Tatsuta Electric Wire & Cable Co., Ltd, Osaka, Japan),

Biomedical Optics EXPRESS

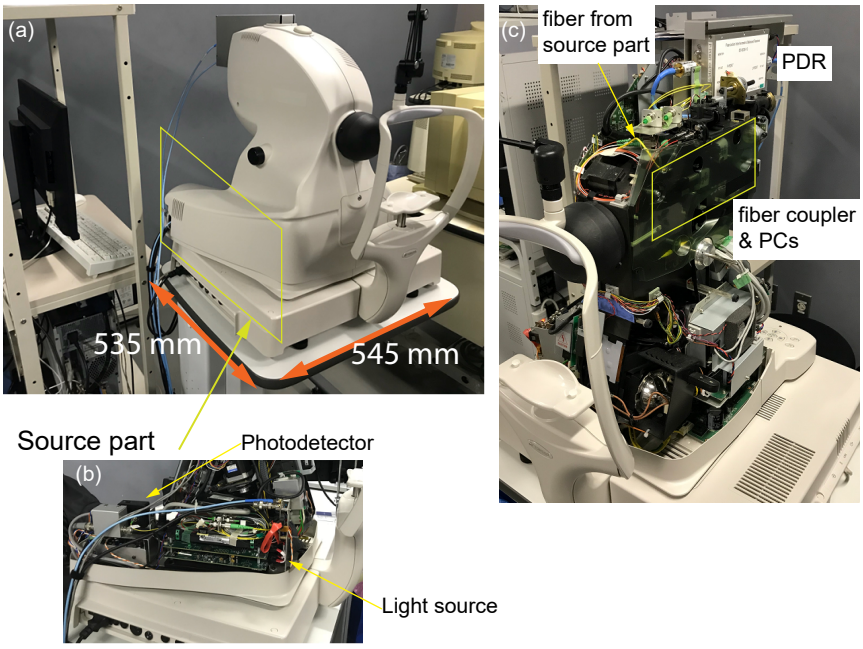


Fig. 2. Pictures of the system. (a) All the components, except the personal computer, are packed into the OCT scanner. (b) The source part, including the light source, FBG, PD and a coupler, is located on the right-hand side of the scanner. (c) Other fiber optic components are attached to the left-hand side of the scanner. The PDR is placed on the top of the scanner.

whereas the remainder of the light is introduced into the interferometer. The reflected light from the FBG is detected by the photodetector (PD). In the interferometer, 20 % of the light is led into the galvanometric scanning mirror system and retinal imaging system. The remaining 80 % is introduced into the reference arm. The probe beam introduced into the eye being scanned has the power of 1 mW on the cornea. The backscattered light is collected and 80 % is directed to the PDR. In the reference arm, light passes through a retro-reflector that includes a dispersion compensation plate. The output of the reference arm is connected to the reference port of the PDR.

The PDR module is a key component with regard to making the PS-OCT compact. A fiber-input PDR module (DE-G036-10, Optohub Co. Ltd., Saitama, Japan) with a size of 156 $\times$ 105 $\times$ 34 mm$^3$ is used. This PDR is similar to that previously introduced for a 1.3-$\mu$m wavelength [28], and designed to work for a 1-$\mu$m wavelength. Two balanced photoreceivers (BPRs) are integrated into the module, which has a bandwidth of 500 MHz and transimpedance gain of $10^4$ V/A. The backscattered light and reference light are led into the module and combined using a non-polarization-sensitive beam splitter. The two combined beams are then split using polarization-sensitive beam splitters and received by the BPRs. The BPR was designed to avoid detecting light that is multiply reflected by optical components inside the BPR, which frequently causes disruptive fixed-pattern noise in swept-source OCTs.

All the components are packed into the OCT retinal scanner, as shown in Fig. 2. The scanner's footprint measures 535 $\times$ 545 mm. There are a pupil camera and fundus monitoring mode with fast OCT scanning, which make it easier to operate the system.

The output voltage from each channel of the PDR passes through a low-pass filter (155 MHz cut-off frequency, SLP-150+, mini-circuit) and a handmade high-pass filter before being recorded

Biomedical Optics EXPRESS

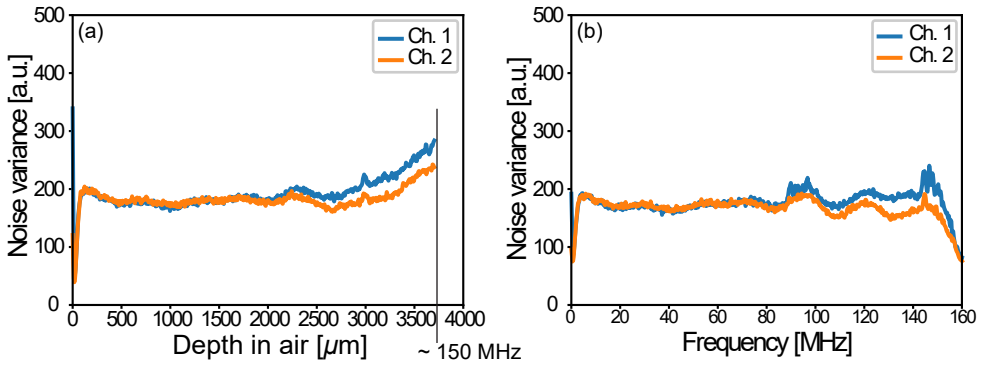


Fig. 3. (a) Depth-dependent background noise statistics with $k$-clock sampling (maximum frequency was approximately 300 MHz). (b) Even temporal sampling with an internal clock of the digitizer (500 MS/s) shows a flat frequency dependency of noise variances. Shaggy spikes at 90 and 145 MHz were caused by residual fixed-pattern noise, and the low-pass filter reduced the noise over 150 MHz.

by a digitizer (ATS9350, Alazar Technologies Inc., Quebec, Canada) with $k$-clock sampling. The output from the PD capturing the reflection from the FBG is amplified and introduced to the digitizer to trigger the recording. Two $k$-linear sampled spectra are windowed, multiplied with a dispersion compensation phase term, and Fourier transformed from spectral domain (k) to spatial domain (z). The median subtraction algorithm [29] is applied to suppress fixed-pattern noise, and the sub-pixel axial shift between the OCT signals of the two channels is corrected. The sensitivity of each polarization channel was measured to be approximately 89.5 dB with a neutral density filter where the attenuation was 19.5 dB (39 dB per round trip). Because the probe power was split across these two polarization channels, it was 3 dB less than a standard OCT without polarization diversity detection. However, the polarization-independent OCT signal was better than that of the standard OCT with 89.5-dB sensitivity, because the polarization-independent OCT was formed by summing two intensity images of two detection polarizations. After the summation of the two intensities, the sensitivity was measured to be 91.0 dB, which was in good agreement with the theoretically expected sensitivity gain of $\sqrt{2} \approx 1.5$ dB. The signal-to-noise ratio (SNR) penalty was measured to be approximately -1.8 dB per 2.4 mm depth. The axial resolution defined by a -3-dB width was measured to be 6 $\mu$m in tissue with a refractive index of 1.38. The $1/e^2$ beam diameter on the cornea was measured as 1.4 mm, and the lateral resolution of the system is expected to be 20 $\mu$m.

## 2.2. DOPU, OCT-A, and OCT computation

### 2.2.1. Noise statistics estimation

The swept source OCT with the $k$-linear sampling clock acquires data nonlinearly in time. It typically causes non-flat noise along the axial direction. The depth-wise estimation of noise statistics is required for the estimators of DOPU (Section 2.2.2) and OCT-A (Section 2.2.3).

Data without backscattered light from tissues are recorded at the end of each volume acquisition while the galvanometric scanning mirror is rotated to direct the probe beam outside the aperture of the retinal scanner. After the reconstruction of the OCT signal (Section 2.1), the obtained complex signals of background data $\tilde{g_{\mathrm{H}}}$ and $\tilde{g_{\mathrm{V}}}$ are used to estimate the noise statistics.

For the complex-based processing (OCT-A and DOPU), the noise variances were estimated as

$$n_{\mathrm{H}}(z) \equiv \left\langle \left| \tilde{g_{\mathrm{H}}}(z,t) - \langle \tilde{g_{\mathrm{H}}}(z,t) \rangle_t \right|^2 \right\rangle_t, \tag{1}$$

Biomedical Optics EXPRESS

and

$$n_{\mathrm{V}}(z) \equiv \left\langle \left| \tilde{g_{\mathrm{V}}}(z,t) - \langle \tilde{g_{\mathrm{V}}}(z,t) \rangle_t \right|^2 \right\rangle_t, \tag{2}$$

where $\langle\rangle_t$ is temporal averaging. A representative example of the estimated noise powers is shown in Fig. 3. The noise variances obtained using $k$-clock sampling increased at locations far from the zero-delay [Fig. 3(a)]. The noise variances between two channels were slightly different, particularly at deep locations. It is likely that the wavelength dependence on the polarization splitting ratio and mismatch of throughput between two polarization channels of the PDR caused this discrepancy. By contrast, the noise variances along the frequency obtained with the internal clock of the digitizer (500 MS/s) were almost flat [Fig. 3(b)]. This shows that irregular temporal sampling using the $k$-clock resulted in the non-flat noise power distribution after Fourier transform.

The intensity of the OCT signal was calculated by first summing the intensities of two polarization channels, and then the summed intensity was averaged across frames, as described in Eq. (5). The intensity calculation [Eq. (5)] was applied to the background data The mean and standard deviation of the intensity of the background data were used as the offset $m_I(z)$ and noise $n_I(z)$ for OCT intensity imaging (Sections 2.2.4).

### 2.2.2. Modified DOPU

To calculate the DOPU, we use an algorithm with a correction for bias caused by background noise [3]. The algorithm is slightly modified from Ref. [3] to account for repeated scans.

The complex OCT signals detected from the H and V channels of the PDR are defined as $g_{\mathrm{H}}$ and $g_{\mathrm{V}}$. Hence, the noise-error-corrected Stokes parameters at each pixel are obtained as

$$\begin{bmatrix} s'_0(x,z,f) \\ s'_1(x,z,f) \\ s'_2(x,z,f) \\ s'_3(x,z,f) \end{bmatrix} = \begin{bmatrix} |g_{\mathrm{H}}(x,z,f)|^2 + |g_{\mathrm{V}}(x,z,f)|^2 - [n_{\mathrm{H}}(z) + n_{\mathrm{V}}(z)] \\ |g_{\mathrm{H}}|(x,z,f)^2 - |g_{\mathrm{V}}(x,z,f)|^2 - [n_{\mathrm{H}}(z) - n_{\mathrm{V}}(z)] \\ 2\,\mathrm{Re}\left[g_{\mathrm{H}}(x,z,f) g^*_{\mathrm{V}}(x,z,f)\right] \\ 2\,\mathrm{Im}\left[g_{\mathrm{H}}(x,z,f) g^*_{\mathrm{V}}(x,z,f)\right] \end{bmatrix}, \tag{3}$$

where $n_{\mathrm{H}}(z)$ and $n_{\mathrm{V}}(z)$ are the measured noise powers for each polarization channel. The details of the measurement and estimation of noise powers, $n_{\mathrm{H}}(z)$ and $n_{\mathrm{V}}(z)$, are described in Section 2.2.1. $x, z$ are indices of a pixel along the lateral and axial directions, respectively. $f$ is the index of the repeated B-scan frame ($f = 1, \cdots, N$). Then, a spatial average of the noise-error-corrected Stokes parameters $\overline{s'_v}(x,z,f)$ ($v$ =0, 1, 2, 3) is calculated with a moving average. Multiple frames are acquired at the same location and combined to suppress noise. The DOPU $d$ with $N$ frames is obtained as

$$d(x,z) = \frac{\sum_{f=1}^{N} \sqrt{\sum_{v=1}^{3} \overline{s'_v}^2(x,z,f)}}{\sum_{f=1}^{N} \overline{s'_0}(x,z,f)}. \tag{4}$$

Instead of a coherent averaging of repeated frames [3], incoherent summation is applied to both the denominator and numerator of Eq. (4).

### 2.2.3. Complex-decorrelation OCT-A

Blood perfusion is contrasted with a complex-decorrelation OCT-A algorithm with noise correction [30]. The temporal correlation coefficient of the OCT signal without additive noise $\bar{r}_{Sf}(\tau; x, z)$ is estimated, where $\tau$ is the time lag to calculate the temporal correlation coefficient. Although the algorithm used here is almost the same as the previous algorithm [30], there are a few differences. The median filtering along the transverse ($x$) direction in the bulk phase shift estimation [Eq. (32) in Ref. [30]] is disabled to estimate the A-line-wise bulk phase shift. The

Biomedical Optics EXPRESS

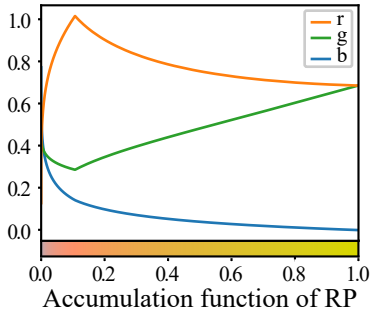


Fig. 4. Lookup table for color coding in pigment and flow imaging. r,g,b: stimulus values for red, green, and blue coordinates.

uncertainties of trigger and $k$-clock timing cause a shift of 1 clock cycle and a relative linear phase change among A-lines [28,31]. Because any clock jitter correction is not used in the current system, this phase change corrupts the complex-decorrelation estimation. Using A-line-wise bulk phase shift correction, the offset of the linear phase change caused by the clock shift is also canceled in the same manner as the bulk motion phase shift. This eases the corruption of the complex correlation estimation caused by the clock jitter. The number of polarization channels $P$ is two (single input × two detection channels). Depth-dependent noise powers [Eqs. (1) and (2)] are used for the estimation because the system with $k$-clock sampling has varying noise power according to the depth (Section 2.2.1).

#### 2.2.4. Polarization-independent OCT

Backscattered light intensity is calculated by summing the OCT signal powers of the two polarization channels. Then, they are averaged over the repeated B-scans, and noise offset $m_I(z)$ (see Section 2.2.1) is removed, as shown in Eq. (5).

$$I(x,z) = \frac{1}{N}\sum_{f=1}^{N}\left[|g_{\mathrm{H}}(x,z,f)|^2 + |g_{\mathrm{V}}(x,z,f)|^2\right] - m_I(z). \tag{5}$$

## 3. Image formation

### 3.1. Cross sections

DOPU values are mapped using a rainbow color map, as is typical for cross-sectional DOPU imaging. Blue is assigned to the DOPU value of zero and the red is assigned to a value of one. The locations for which $d^{-1} < 1$ are shown in red. Although the color DOPU image demonstrates good contrast for low DOPU distribution, it is difficult to interpret its location relative to the structure. For display, the color DOPU image is composed using the log-scaled OCT intensity. The color space of the DOPU image is converted to the hue, lightness, saturation color space and then the saturation plane is replaced with the log-scaled OCT intensity. The low-intensity region approaches gray in this image.

Cross-sectional OCT-A images are displayed in grayscale with the estimated correlation coefficient $\overline{r}_{Sf}$. Low correlation corresponds to high perfusion. Hence, the pixel exhibited a decorrelation coefficient value (1 - $\overline{r}_{Sf}$) of one is assigned to white and the value of zero is assigned to black. Locations for which $\overline{r}_{Sf}^{-1} < 1$ are represented as black.

Biomedical Optics EXPRESS

### 3.2. En face pigment and flow imaging

RPE abnormalities are difficult to detect in *en face* DOPU projections hinders the visualization of DOPU changes of the very thin RPE layer. Hence, some RPE segmentation methods are required to map the RPE abnormalities. In clinical ophthalmology, a gold standard tool for RPE abnormality mapping is fluorescein angiography, which detects fluorescence generated by fluorescent dyes injected into the patient's vein. Thus, it measures fluorescence from choroidal vessels which is attenuated by the RPE melanin [32]. A combination of DOPU and OCT-A, that is, melanin and blood flow contrasts, could be a suitable solution for mapping RPE abnormalities. We use an *en face* projection image construction method using DOPU and OCT-A; so-called "pigment and flow" (PAF) imaging [30].

We use OCT-A and DOPU to create the color *en face* image as

$$\mathbf{E}(x, y) = \sum_{z} \{1 - \mathrm{M}[\overline{r}_{Sf}(\tau; x, y, z)]\} A^{\alpha}(x, y, z) \cdot \mathbf{C}[A(x, y, z)], \tag{6}$$

where

$$\mathrm{M}[x] = \begin{cases} x, & \text{if } x^{-1} > 1. \\ 1, & \text{otherwise.} \end{cases} \tag{7}$$

$A(x, y, z) = \exp\left[-\Delta z \sum_{i=0}^{z} \mathrm{Med}\{1 - \mathrm{M}[d(x, y, i)]\}_{(x,y,i)}\right]$ is an accumulation function of the randomness of the polarization state, which is unity at the surface (z = 0). $\mathrm{Med}\{\}_{(x,y,z)}$ is a three-dimensional median filter. In this study, the 3 × 3 × 3 cross structuring element of the median filter is used. The accumulation function $A$ decreases when the axial integration range includes a low DOPU region. By integrating infinite low DOPU regions, $A$ becomes zero.

The color lookup table $\mathbf{C}(x) = [R(x), G(x), B(x)]^T$ was designed to have a linear relationship between the color difference and change in DOPU integration $\Delta z(1 - \mathrm{M}[d(x, y, z)])$ [30]. To apply summation $\sum_z$, that is, the color addition, $\mathbf{C}$ is represented in sRGB color space before gamma transformation (Fig. 4). The term $A^{\alpha}$ is the weight of the OCT-A signal depending on the DOPU accumulation function $A$. This term works as a sort of depth cueing, and parameter $\alpha$ modifies the balance between OCT-A signals above and below pigmented tissues. In this study, $\alpha$ = 0.01 is used. After axial summation [Eq. (6)], the *en face* data $\mathbf{E}$ is normalized by the [99.9, 5] percentile in intensity $[(R + G + B) / 3]$, and then the sRGB gamma transformation is applied.

The retinal region normally exhibits no melanin; hence, the retinal vessels appear as a yellowish color. In the case of the choroid, the region between the choroidal vessel and surface includes the RPE and choroidal stroma, which are melanin-rich tissues. The accumulation function $A$ becomes lower than one, and therefore, the choroidal vessels appear as orange to blue. This characteristic of DOPU allows the discrimination of the retinal and choroidal vasculature according to different colors. If abnormalities in RPE cause reduced melanin or melanin loss, then this discrimination fails. Hence, RPE abnormalities appear as abnormal colors in the blood flow signal.

## 4. Results

The developed clinical prototype of the PAF-OCT system was installed in Tokyo Medical University Ibaraki Medical Center, and healthy eyes and some posterior pathologic cases were imaged. The present study adhered to the tenets of the Declaration of Helsinki and was approved by the Institutional Review Boards of Tokyo Medical University. The nature of the present study and the implications of participating in this research project were explained to all study participants, and written informed consent was obtained from each participant before any study procedures or examinations were performed.

The scanning protocol consisted of four repeated horizontal scans with 512 A-lines × 256 locations along the vertical direction. The acquisition of one volume took 6.5 s, and the scanning area was 6 × 6 $mm^2$. The kernel size for the DOPU calculation was 3 × 3 pixels, which was

Biomedical Optics EXPRESS

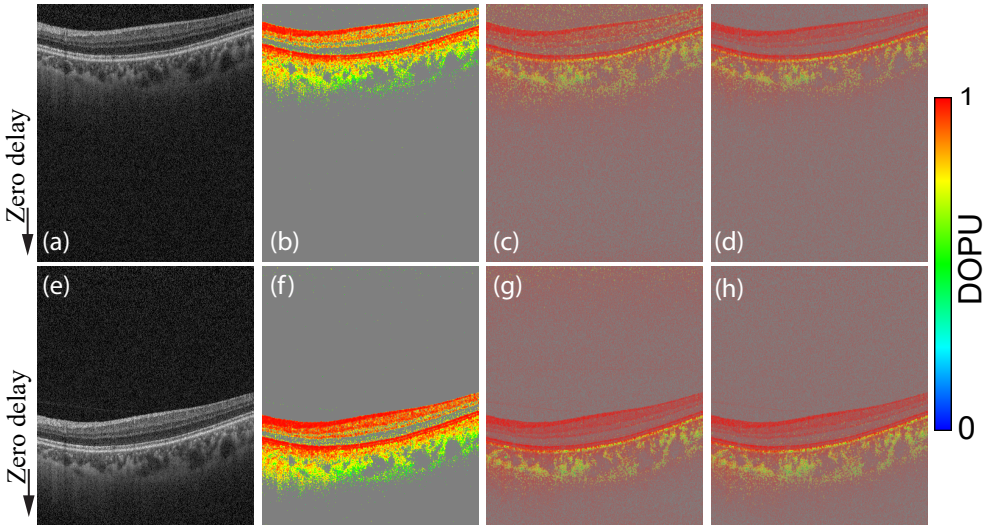


Fig. 5. Cross-sectional OCT intensity and DOPU images of a human eye. The lateral scanning range was 6 mm, and the axial range was 2.6 mm in tissue. Images at two locations are shown (a–d: far from the zero delay, e–h: near to the zero delay). Without noise correction (b, f, below 8 dB SNR region was masked), DOPU values decreased in low SNR regions (i.e., the ganglion cell layer, and inner nuclear layer). Noise-corrected DOPU (c, g) removed the bias at near zero delay; however, single-depth noise estimation could not correct the bias far from the zero delay. Noise-correction method using an axial profile of noise power (d, h) removed the bias for all imaging depths.

35 $\mu$m and 13 $\mu$m along the lateral and axial directions, respectively. The kernel size for the OCT-A process was 3 pixels for complex averaging along the axial direction and three A-lines for covariance averaging along the lateral direction [30].

### 4.1. Noise-corrected multi-contrast imaging

Cross-sectional images of DOPU (Fig. 5) and OCT-A (Fig. 6) obtained from a healthy eye at a different distance from the zero-delay (top row: far; bottom row: near). DOPU and OCT-A were processed without noise correction (second column), with noise correction by single-depth noise estimation (third column), and noise correction using an axial noise profile (fourth column). Without noise correction [Figs. 5(b), 5(f), 6(b), and 6(f)], DOPU and decorrelation values depended on the SNR; hence, low SNR regions, such as the ganglion cell layer and inner/outer nuclear layers, exhibited low DOPU and high decorrelation values, even though there was no melanin and blood flow. Additionally, DOPU and decorrelation values in these low SNR regions changed between different imaging depth locations. Near the zero delay, noise correction by single-depth noise estimation worked well because the noise power was almost constant in this region [Figs. 5(g) and 6(g)]. However, DOPU and OCT-A were biased when the imaging location was far from the zero delay [Figs. 5(c) and 6(c)]. This is because of the high noise power at such locations in comparison with other depths (Fig. 3). Noise estimation at every depth (Section 2.2.1) was necessary to correct the bias at every depth, and provided stable imaging results [Figs. 5(d), 5(h), 6(d), and 6(h)].

### 4.2. Repeatability of DOPU imaging

To confirm the repeatability of DOPU imaging, both eyes of two subjects were scanned sequentially, and then this operation was iterated five times. Hence, the system was realigned at each acquisition.

Biomedical Optics EXPRESS

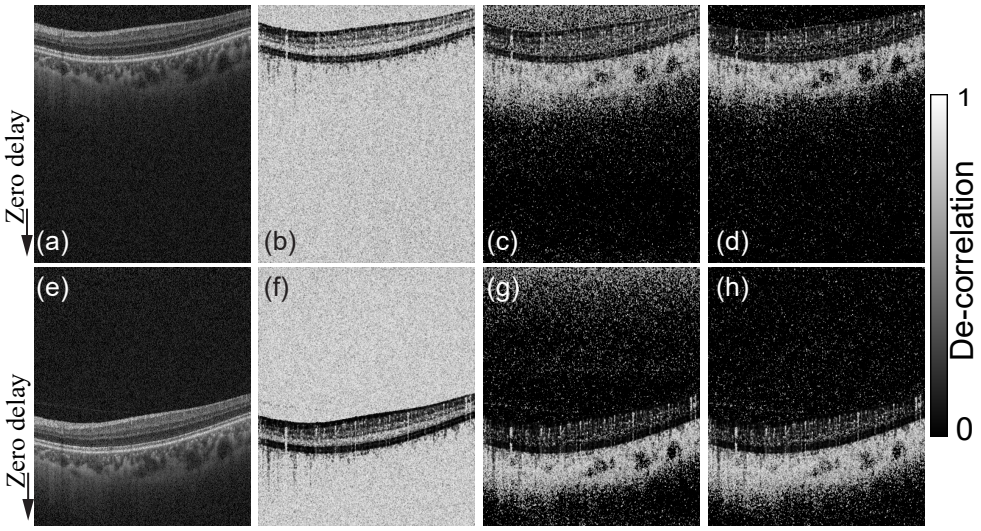


Fig. 6. Cross-sectional OCT intensity and OCT-A images of a human eye. The lateral scanning range was 6 mm and the axial range was 2.6 mm in tissue. Images at two locations are shown (a–d: far from the zero delay, e–h: near to the zero delay). Without noise correction (b, f), decorrelation values decreased in low SNR regions (i.e., the ganglion cell layer, inner nuclear layer, and outer nuclear layer). Noise-corrected OCT-A (c, g) removed the bias at near zero delay; however, single-depth noise estimation could not correct the bias far from the zero delay. Noise-correction method using an axial profile of noise power (d, h) removed the bias for all imaging depths.

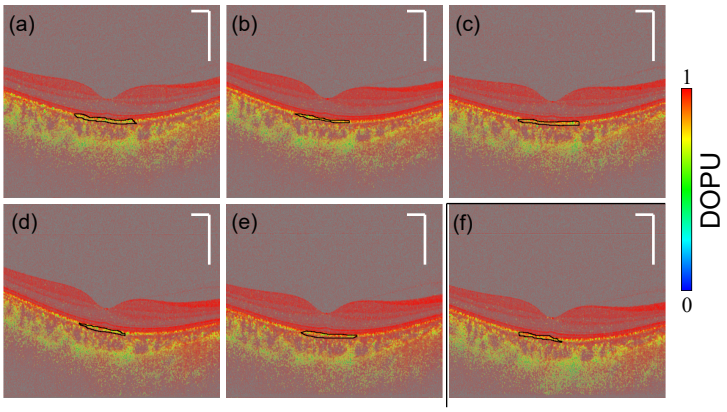


Fig. 7. Repeated measurement results of DOPU imaging with the right eye of Subject 1. (a–e) DOPU images of five repeated measurements. (f) DOPU image obtained 2 months previously. The repeatability of the visualization was high. The mean values of DOPU of the RPE at the fovea (enclosed by black curves) were used for statistical analysis (Section 5.1). The scale bar indicates 500 $\mu$m.

Biomedical Optics EXPRESS

Table 1. Repeated measurement results of DOPU. Averaged values of DOPU at delineated RPE. The standard deviation is in parentheses.

| ID | Subject 1, right | Subject 1, left | Subject 2, right | Subject 2, left |
|---|---|---|---|---|
| 1 | 0.839 (0.096) | 0.843 (0.100) | 0.851 (0.093) | 0.859 (0.093) |
| 2 | 0.847 (0.075) | 0.855 (0.105) | 0.878 (0.080) | 0.859 (0.107) |
| 3 | 0.871 (0.091) | 0.847 (0.076) | 0.859 (0.092) | 0.878 (0.087) |
| 4 | 0.839 (0.112) | 0.859 (0.101) | 0.871 (0.080) | 0.824 (0.109) |
| 5 | 0.882 (0.090) | 0.859 (0.092) | 0.859 (0.083) | 0.859 (0.081) |
| 2 mo previously | 0.882 (0.084) | | | |

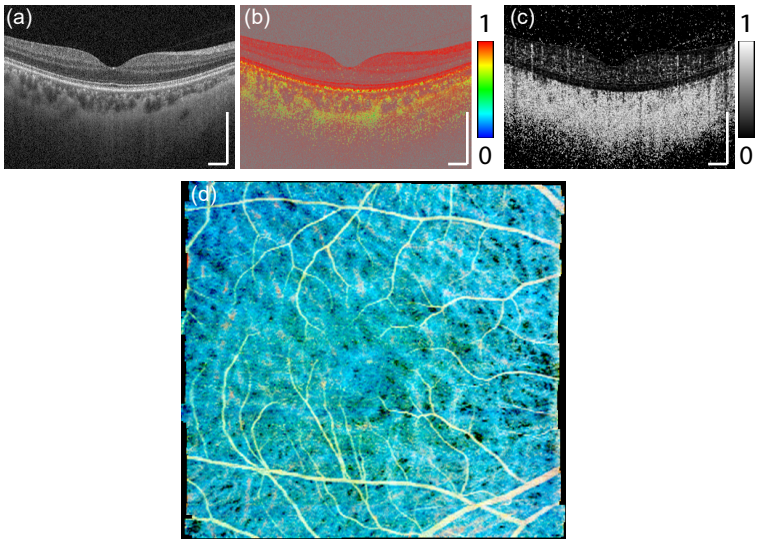


Fig. 8. Healthy human macular imaging results. Cross-sectional (a) OCT, (b) DOPU, and (c) OCT-A images obtained using horizontal scans near the fovea show structural, vascular, and melanin distributions. (d) Pigment and flow image. The scanning range was $6 \times 6$ mm$^2$. The scale bar indicates 500 $\mu$m.

Figure 7 shows the DOPU images of the right eye of Subject 1 for each iteration. This eye was also scanned 2 months previously, and all images visualized a similar low DOPU distribution at the RPE and choroid. The averaged values of DOPU of the delineated RPE at the fovea are presented in Table 1. The Friedman test, which is one-way repeated measures analysis by ranks was applied to five iterated measurements of four eyes. The $p$-value was 0.373 ($> 0.05$); hence, the null-hypothesis (repeated measurement results were sampled from the same mother group) was not rejected. A statistically significant difference between repeated measurements was not found.

### 4.3. *Normal healthy eye*

A healthy volunteer's eye was scanned using the developed system. Cross-sectional OCT, DOPU, and OCT-A B-scan images of the posterior part of the eye are shown in Figs. 8(a)–8(c). The morphological structure, vasculature, and melanin distribution were thereby obtained. The PAF image [Fig. 8(d)] visualized the retinal and choroidal vasculature simultaneously in different colors according to the location of these vascular networks relative to the pigment rich tissues,

Biomedical Optics EXPRESS

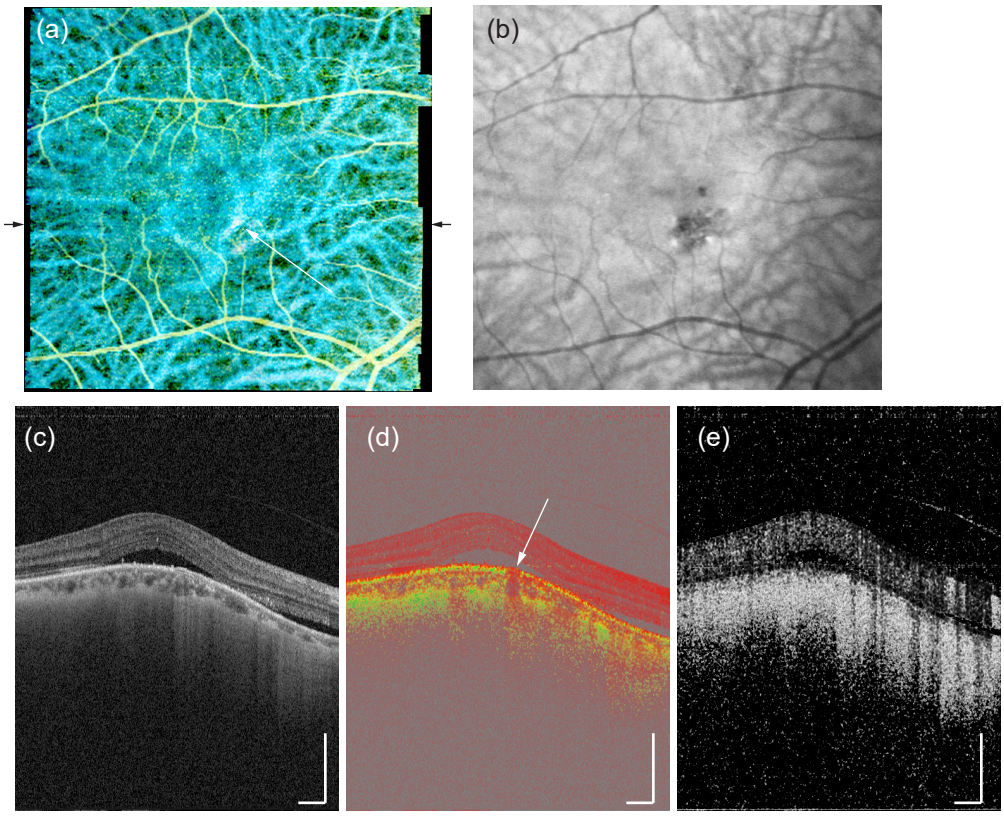


Fig. 9. Imaging results from a central serous chorioretinopathy patient. (a) *En face* PAF and (b) near-infrared autofluorescence image. Cross-sectional (c) OCT, (d) DOPU, and (e) OCT-A images obtained for horizontal scans at the location indicated by black arrows in (a). The PAF image (a) and DOPU cross section (d) show the low pigmentation (white arrows). The scanning range was $6 \times 6$ mm$^2$. The scale bar indicates 500 $\mu$m.

that is, the RPE and choroid.

The *en face* PAF image was created by stitching sub-strips of three volumes using the "MosaicJ" plugin [33] of Fiji [34]. Each volume was split by discarding highly decorrelated B-scans. For each B-scan, the complex decorrelation among the pixels that had an SNR greater than 9.5 dB was averaged, and the B-scans that exhibited high averaged decorrelation greater than 0.5 were removed. All PAF image strips of sub-volumes were loaded by "MosaicJ," then rough manual alignment and automatic fine alignment were applied.

### 4.4. Pathological eye imaging

The pigment and flow images, and cross sections of each contrast of a central serous chorioretinopathy patient are shown in Fig. 9. The images were from the right eye of a 67-year-old female. Abnormal flow signals were apparent in the macular region in the PAF image [white arrow in Fig. 9(a)]. The cross-sectional DOPU image [Fig. 9(d)] shows a lack of RPE pigmentation at the corresponding location. In the OCT cross section [Fig. 9(c)], the RPE layer appeared as a smooth layered structure, and the signal magnitude at the abnormal location was similar to that of surrounding regions. If the RPE structure was carefully observed, it was possible to

Biomedical Optics EXPRESS

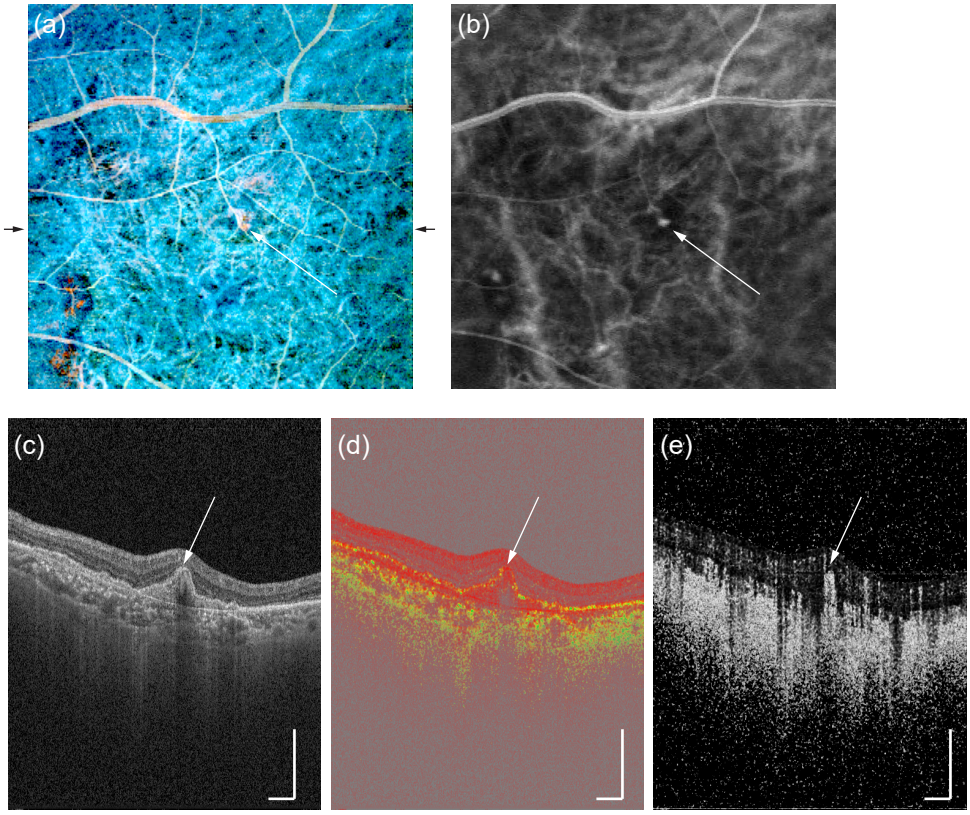


Fig. 10. Imaging results from a PCV patient. (a) *En face* PAF and (b) indocyanine green angiography images. Cross-sectional (c) OCT, (d) DOPU, and (e) OCT-A images were obtained using horizontal scans at the location indicated by black arrows in (a). The PAF image (a) and DOPU cross section (d) show the low pigmentation (white arrows). The scanning range was $6 \times 6$ mm$^2$. The scale bar indicates 500 $\mu$m.

detect that the RPE at the defective location was slightly detached from the basement membrane. However, it was difficult to determine this using only the OCT cross sections. This RPE defect was confirmed using a near-infrared autofluorescence image [Fig. 9(b)] obtained using a scanning laser ophthalmoscope (HRA, Heidelberg Inc.). Note that the *en face* PAF image [Fig. 9(a)] was created by stitching sub-strips of two sequential volumes using the "MosaicJ" plugin [33] of Fiji [34] as same as Section 4.3.

Images of a polypoidal choroidal vasculopathy (PCV) patient are shown in Fig. 10. The images were from the left eye of a 66-year-old male. An abnormal flow signal were found in the PAF image superior to the macula [white arrow in Fig. 10(a)]. Figure 10(b) shows an indocyanine green angiography (ICGA) image, which contrasts fluorescent dyes injected into a vein. The location of the abnormal signal in the PAF image was collocated with hyper-fluorescence in the ICGA [white arrow in Fig. 10(b)]. The cross-sectional images at this location [indicated by black arrows in Fig. 10(a)] show RPE elevation and exudation. The RPE may be defected according to the decreased pigmentation (high DOPU). Melanin seemed to disappear at the top of the RPE elevation [Fig. 10(d)], and an abnormal flow signal was apparent under the elevated RPE layer [Fig. 10(e)].

Biomedical Optics EXPRESS

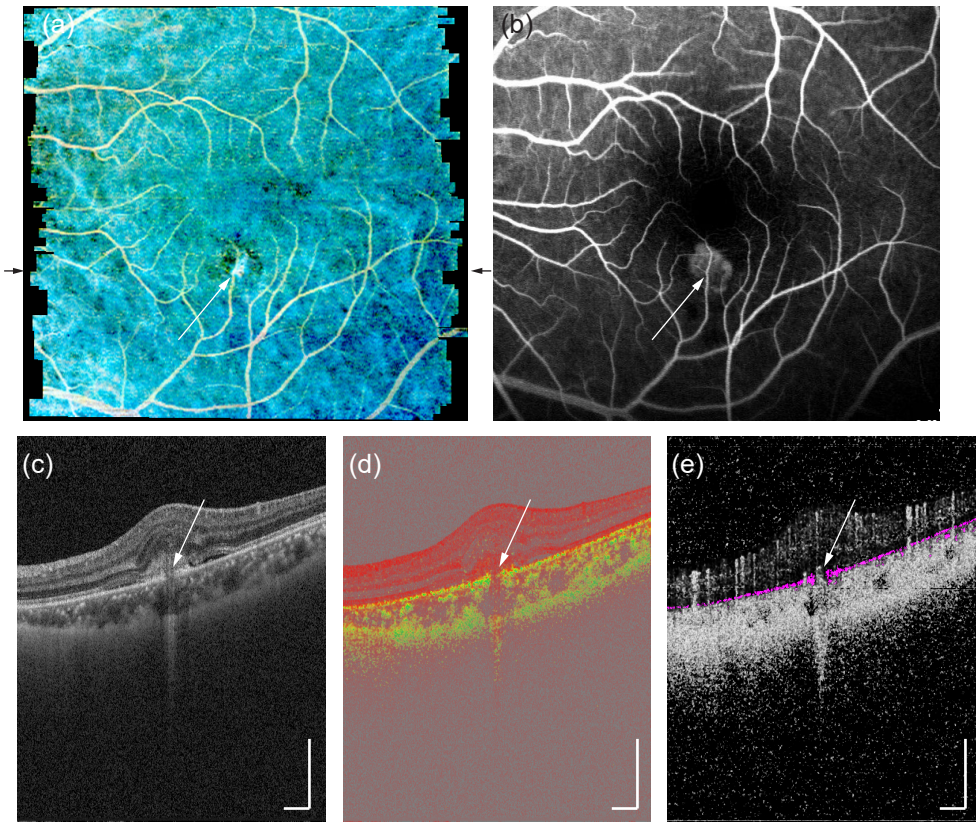


Fig. 11. Imaging results from a CNV patient. (a) *En face* PAF and (b) fluorescein angiography images. Cross-sectional (c) OCT, (d) DOPU, and (e) OCT-A images were obtained using horizontal scans at the location indicated by black arrows in (a). The segmented RPE is shown in magenta (e). The scanning range was $6 \times 6$ mm$^2$. The scale bar indicates 500 $\mu$m.

Images of a choroidal neovascularization (CNV) patient are shown in Fig. 11. The images were from the right eye of a 26-year-old female. An abnormal yellow blood flow signal was apparent in the PAF image [Fig. 11(a)], as indicated by the white arrow. The location of the abnormal signal corresponded to hyper-fluorescence in the fluorescein angiography [white arrow in Fig. 11(b)]. OCT, DOPU, and OCT-A cross sections indicated exudation, RPE damage, and neovascularization [white arrows in Figs. 11(c)– 11(e)]. The pixel-wise segmentation algorithm of the RPE [35] was applied. The pixels segmented as RPE are shown in magenta [Fig. 11(e)]. The neovascularization existed above the RPE line; hence, the CNV could be classified as type 2. Note that the *en face* PAF image [Fig. 11(a)] was created by stitching sub-strips of three sequential volumes using the "MosaicJ" plugin [33] of Fiji [34] in the same manner as Section 4.3.

These imaging results from pathological cases show that the clinical prototype system had the ability to detect RPE abnormalities with DOPU imaging. The simple combination of DOPU and OCT-A provided an *en face* PAF image, that was suitable for mapping RPE and vascular abnormalities.

Biomedical Optics EXPRESS

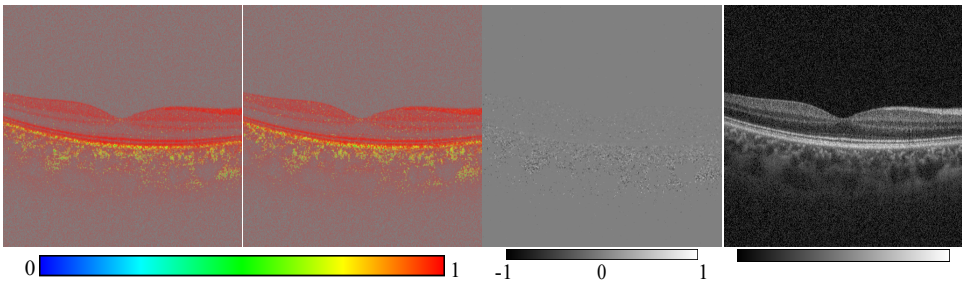


Fig. 12. DOPUs in Jones-matrix OCT. (a), (b) DOPUs calculated from two orthogonal input polarization states, (c) difference image of the DOPUs of two inputs, and (d) OCT cross section.

## 5. Discussion

### 5.1. Input polarization state

In this paper, the PAF-OCT used a single input polarization state to calculate the DOPU. Our previous studies of DOPU used two orthogonal input polarization states of the Jones-matrix OCT (JM-OCT). Figure 12 shows retinal OCT and DOPU cross sections obtained using 1-$\mu$m JM-OCT [36]. The two DOPUs obtained from the orthogonal input polarization states [Figs. 12(a) and 12(b)] are similar to each other [Fig. 12(c)]. The root-mean-square error of the images is 0.037. Hence, it can be said that the PAF-OCT using a single input polarization state could obtain DOPU comparable with that obtained using the previous method [3] for JM-OCT when the same or orthogonal input polarization state was used.

It is well known that the degree of polarization depends on the input polarization state. Similarly, the input state dependence of RP has been reported [37, 38]. The fluctuation of the input polarization state will make DOPU imaging unrepeatable. In the developed system, all fiber components were loaded on the scanning stage (Fig. 2); hence, no optical SM fiber moved during operation. This resulted in the high repeatability of DOPU imaging, as shown in Section 4.2. This result supports the good repeatability of DOPU imaging.

Using an SM fiber in the sample arm, the polarization state on the sample became unknown. Hence, the input polarization state was unoptimized for DOPU imaging. However, the posterior part of the eye is located behind the cornea, which is birefringent. The corneal retardation and optic axis orientation have variations among individuals [39,40]. Double-pass corneal retardation values ranging from 0 to 190 nm with a 585 nm wavelength have been reported for 73 subjects [39]. This may correspond to single-pass phase retardation for a 1-$\mu$m wavelength ranging from 0 to approximately $\pi/5$ radians. This individual variation of corneal retardation may produce a substantial, uncontrolled polarization state change. Additionally, there are fibrous tissues anterior to the pigment tissue, that is, a nerve fiber layer and Henle's fiber layer [41–43]. Hence, the polarization state of the probe beam at the melanin in the posterior eye is also unknown, even if the polarization state in the optical system is controlled. To optimize the contrast of DOPU for each individual eye, compensation for the polarization state change caused by birefringence of these tissues, at least the cornea, will be required. Despite this, a single input polarization state is used in several applications and the results seem to be promising [8–13]. Hence, the imaging of DOPU using a stable packaged SM fiber-based OCT system with a PDR and a single input polarization state may be applicable for clinical applications.

Biomedical Optics EXPRESS

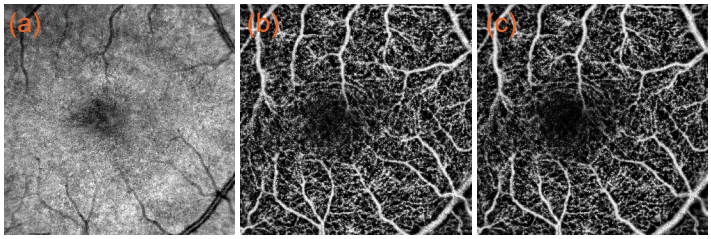


Fig. 13. (a) OCT and (b, c) retinal OCT-A projections obtained using the Lissajous scanning protocol show a motion-free *en face* posterior eye structure and retinal vasculature. Retinal OCT-A (b) was obtained using the projection of OCT-A weighted by the accumulation function of DOPU, that is, without layer segmentation. Retinal OCT-A (c) was created from the slab of OCT-A volume by delineating the segmentation results of the inner limiting membrane and RPE. The scanning range was $3 \times 3$ mm$^2$.

### 5.2. Retinal OCT-A

We introduced a PAF image, which is a combination of DOPU and OCT-A, to visualize abnormalities of melanin pigmentation and vasculature simultaneously. Furthermore, DOPU can be used to assist OCT-A imaging. For example, retinal vasculature imaging with OCT-A requires the exclusion of tissues below the RPE to exclude the choroidal blood flow signal. As the choroidal blood flow signal is strong and broad along the axial direction, the projection of an entire OCT-A volume dims the thin retinal microvasculature. A simple method that is just a weighted projection of OCT-A with the accumulation function $A$ is introduced as

$$\mathrm{OCTA}_{\mathrm{retina}} = \sum_{z} \{1 - \mathrm{M}[\bar{r}_{Sf}(\tau; x, y, z)]\} A(x, y, z). \tag{8}$$

This *en face* map visualizes almost only retinal vasculature, without layer segmentation.

Figure 13 shows *en face* projections of OCT [13(a)], OCT-A with DOPU weighting [13(b)], and OCT-A with layer segmentation [13(c)]. The retinal *en face* OCT-A image with segmentation [Fig. 13(c)] was obtained by integrating 1 - M[$\bar{r}_{Sf}$] between the inner limiting membrane and RPE, which were defined using a segmentation algorithm [44]. Both OCT-A images were displayed after contrast limited adaptive histogram equalization. The retinal *en face* OCT-A with DOPU weighting [Eq. (8)] shows clear retinal microvasculature [Fig. 13(b)] that is the same as OCT-A image with retinal layer segmentation [Fig. 13(c)]. The DOPU weighted retinal *en face* OCT-A allowed the clear visualization of retinal microvasculature without retinal layer segmentation. The eye motion was corrected using previous method [45]. A modified Lissajous scanning pattern with two repeated cycles with 724 A-lines and 724 cycles (two periods of Lissajous pattern) was used. The acquisition took 10 s. For the DOPU calculation, three A-lines along the scanning direction $\times$ 3 pixels (13 $\mu$m) along axial directions were used. The kernel size for OCT-A processing was 5 pixels (21.6 $\mu$m) along the axial direction for complex averaging. Because the acquisition time was long, the subject blinked once during the scan; however, the Lissajous motion correction algorithm tolerated the blink and removed and filled blank scanning cycles [45]. Motion-free *en face* views of the posterior part of the eye and retinal vasculature were obtained.

## 6. Conclusion

We developed a clinical prototype device for PAF-OCT and demonstrated retinal pathology imaging. The simplified scheme used components that were easy to pack into a compact housing.

Biomedical Optics EXPRESS

The demonstrations of retinal pathology imaging suggest possibilities for a wide range of applications in clinical ophthalmology, although the additional contrast was only RP.

## Funding

Japan Society for the Promotion of Science (JSPS) KAKENHI (15K13371, 17K14121); Ministry of Education, Culture, Sports, Science and Technology (MEXT) through the Program for building Regional Innovation Ecosystems.

## Acknowledgments

We acknowledge Optohub for its great effort in building the compact polarization diversity receiver.

## Disclosures

SM: Nidek (F), Tomey Corporation (F, P), Kao (F); SA: Nidek (F), Tomey Corporation (F), Kao (F); YY: Nidek (F), Tomey Corporation (F, P), Kao (F); TM: Topcon (E); TY: Topcon (E); MM: Allergan (F), Alcon (F), Novartis (F,R), Santen (F,R), Bayer(F).